Project No. 10-924

Fission Product Transport in TRISO Particle Layers under Operating and Off-Normal Conditions

Reactor Concepts R&D

Dr. Anton Van der Ven
University of Michigan

In collaboration with:
Drexel University

Madeline Feltus, Federal POC
Phil Winston, Technical POC

NEUP Nuclear Energy University Programs
U.S. Department of Energy

QUARTERLY PROGRESS REPORT

Project Title: Fission Product Transport in TRISO Particle Layers under Operating and Off-Normal Conditions

Covering Period: July 1, 2013 through Sept. 30, 2013
Date of Report: April 26, 2014
Recipient: University of Michigan
2300 Hayward Street
Ann Arbor, MI 48109-2104
Award Number: 103195
Project Number: 10-924
Principal Investigator: Anton Van der Ven, 805-893-7920, avdv@engineering.ucsb.edu
Co-PIs: Gary S. Was, 734 763-4675, gsw@umich.edu
Lumin Wang, lmwang@umich.edu
Mitra Taheri, mtaheri@coe.drexel.edu

Objective: *The objective of this project is to determine the diffusivity and chemical behavior of key fission products (Ag, Cs, I, Te, Eu and Sr) through SiC and PyC both thermally, under irradiation, and under stress using FP introduction techniques that avoid the pitfalls of past experiments.* The experimental approach is to create thin PyC-SiC couples containing the fission product to be studied embedded in the PyC layer. These samples will then be subjected to high temperature exposures in a vacuum and also to irradiation at high temperature, and last, to irradiation under stress at high temperature. The PyC serves as a host layer, providing a means of placing the fission product close to the SiC without damaging the SiC layer by its introduction or losing the FP during heating. Experimental measurements of grain boundary structure and distribution (EBSD, HRTEM, APT) will be used in the modeling effort to determine the qualitative dependence of FP diffusion coefficients on grain boundary orientation, temperature and stress.

Background: Containment of fission products (FP) within the TRISO fuel particles is critical to the success of the Very High Temperature Reactor (VHTR). In these particles, the SiC shell provides structural support and acts as the main fission product barrier. While the behavior of several fission products is of interest, including Ag, Cs, I, Te, Eu and Sr, the fission products Ag and Cs appear to be able to penetrate the SiC layer most easily. Between 82-100% of Ag was released in US coated particle fuel depending on the fuel form (UC_2, UCO or UO_2) and SiC grain morphology (equiaxed or columnar), and up to 24% of Cs was released in the same fuel. An understanding of the diffusion of fission products through SiC is needed, not only to determine how it occurs so that mitigation measures can be devised, but also to model FP transport in fuel performance codes in order to provide more accurate fuel behavior modeling in both normal and off-normal operating conditions.

1. Introduction

An understanding of the transport mechanisms of fission products through SiC is required not only to determine how it occurs so that mitigation measures can be devised, but also to support fuel performance codes [1,2] and provide for more accurate fuel behavior modeling in both normal and off-normal operating conditions. Containment of fission products (FP) within the TRISO fuel particle is critical to the success of the Very High Temperature Reactor (VHTR). The SiC layer of TRISO particles provides both structural support and serves as the primary diffusion barrier for FPs at temperatures up to 1300ºC during operation.

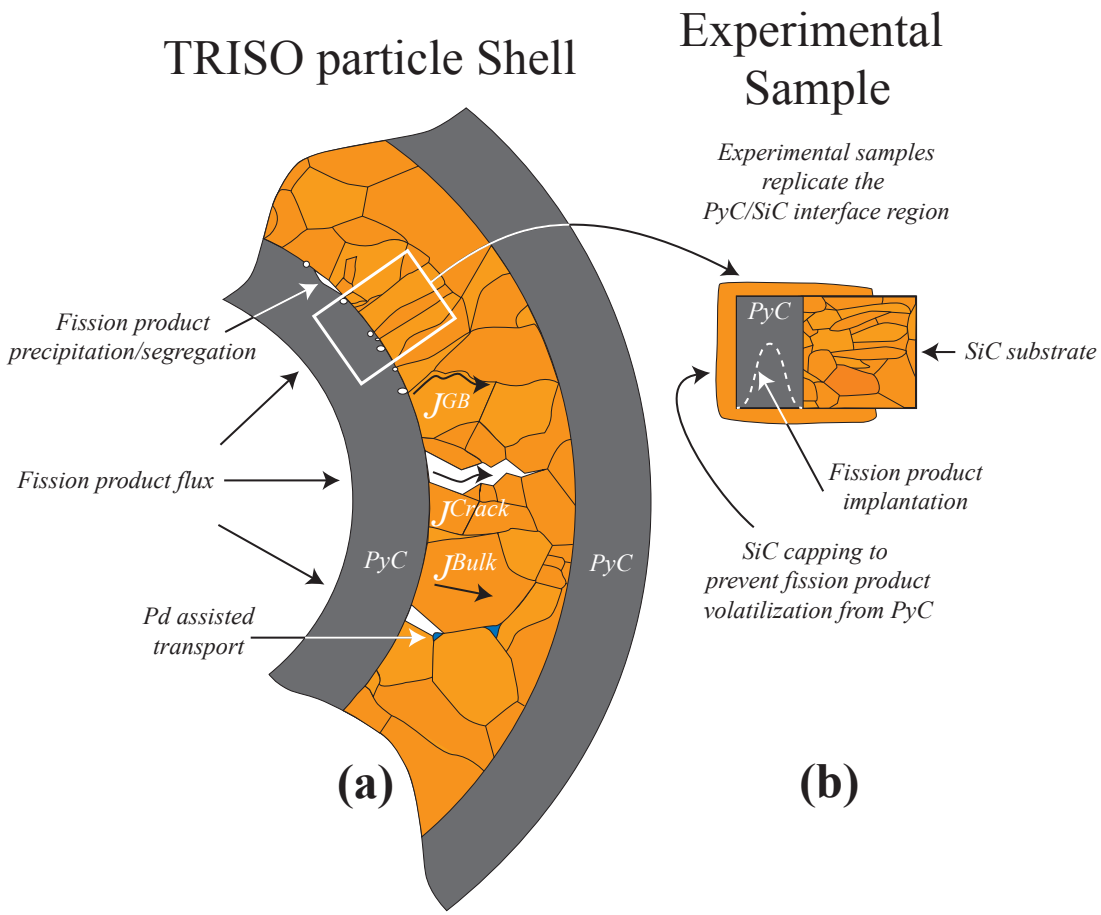

Figure 1. **(a)** The TRISO particle shell illustrating various mechanisms for fission product transport through SiC. Four possible mechanisms of FP escape include: (i) bulk diffusion through grains, (ii) grain boundary diffusion, (iii) diffusion along interconnected micro/nano cracks, and (iv) Pd-assisted FP transport. **(b)** A schematic of our unique sample that replicates the PyC/SiC heterostructure, in which FP are implanted in the PyC, thereby avoiding implantation damage in SiC or non-realistic FP films. The heterostructure is capped with SiC to prevent volatilization of the implanted FP at high temperature.

There are many pathways through which fission products could potentially escape through the TRISO particle shell. **Figure 1** illustrates the most important mechanisms that have been a focus of this research. Based on existing evidence from the published literature [1,3,4,5] and evidence generated in the course of this project, we identify four highly likely pathways/mechanisms that could potentially mediate FP escape.

1. **Bulk diffusion:** The majority of the SiC volume is made up of grains, which each individually constitutes a single crystal. Fission product diffusion through the bulk of the SiC crystal is therefore an obvious potential pathway for their escape.
2. **Grain boundary diffusion:** While grain boundaries represent a substantially smaller fraction of the volume of the SiC layer, their more open structure along with the disruption in bonding can raise the local thermodynamic solubility of fission products (through segregation) as well as their mobility.
3. **Fission product transport along preexisting nano-cracks:** If nano or micro cracks are present, they would constitute very fast short-circuit diffusion pathways for fission products. Transport along interconnected crack networks can occur either through surface diffusion, or in gaseous form.
4. **Palladium assisted FP transport:** Experimental and theoretical evidence suggests that Pd may facilitate fission product transport in SiC. It is well known that Pd has a corrosive effect on SiC and recent studies of TRISO particles have detected Pd precipitates at grain boundary junctions. Furthermore, our own first-principles analysis of decohesion in SiC has shown that Pd acts as an embrittling agent of SiC, dramatically lowering the maximum stress of decohesion. Any resultant nano/micro-cracks due to Pd embrittlement can then serve as pathways for other FPs to escape. Pd segregation and precipitation along grain boundaries may also facilitate FP diffusion along these grain boundaries, as the solubility of fission products such as Ag is higher in Pd than in SiC.

All four mechanisms are likely to be enhanced by ***irradiation***. Irradiation can dramatically alter transport mechanisms due to the damage it produces. It may exacerbate particular mechanisms that mediate FP transport more than others.

Summary of accomplishments

We briefly summarize accomplishments and new insights that have been generated in the course of this project. There was a sizable experimental component as well as a computational component relying on first-principles electronic structure methods.

As experimental accomplishments, we were successful in:

- Developing a method of depositing PyC onto SiC and implanting Ag, Cs, I, Eu, Sr, and Pd into the PyC layer at realistic compositions and in a geometry that mimics the TRISO particle. This geometry is ideal for studying fission product transport through the PyC, the PyC-SiC interface and SiC.
- Developing a unique capability to fully cap a PyC/SiC multi-layer with SiC to retain FPs during high temperature annealing studies. Such studies have revealed a tendency of Ag to segregate to the PyC/SiC interface, consistent with predictions of our first-principles calculations that Ag does not dissolve in graphite and has a thermodynamic tendency to segregate to the SiC surface.
- Verifying that the high temperature behavior of Ag, Cs, I, Eu, Sr, and Pd in PyC is consistent with that expected from phase diagrams and thermodynamic calculations.
- Developing a capability to irradiate the heterostructures with ions in a highly controlled manner and verifying that the irradiation behavior of Ag in PyC is substantially different from the thermal behavior with significant dynamic solubility.

By relying on first-principles electronic structure calculations, we were able to generate insights about likely pathways and mechanisms with which fission products can escape through the SiC shell of TRISO particles. Our first-principles calculations as well as calculations published by others during the time frame of this project predict that diffusion of fission products through the bulk is unlikely since fission product solubilities in SiC are predicted to be exceedingly low. Our calculations have also shown that fission products such as Ag do not have a tendency to segregate to stacking faults. While fission products such as Ag have an energetic tendency to segregate to grain boundaries relative to bulk SiC, there is still an enormous energy penalty relative to Ag precipitated out in metallic form. Our first-principles calculations, however, did indicate that fission products such as Ag, I, Cs and Sr have an energetic preference to adsorb on SiC surfaces (relative to precipitating out). This suggests that any cracks with newly exposed SiC surfaces will serve as a thermodynamically viable pathway for fission product escape.

Our discovery of the thermodynamic tendencies of fission products to segregate to SiC surfaces led us to explore mechanisms with which internal surfaces could be created. In this context, we explored the role of Pd in embrittling SiC. A thermodynamic analysis of first-principles calculated cohesive energies with and without Pd showed that Pd can readily decrease the maximum stress of decohesion of SiC by a factor of 3. The presence of Pd therefore will tend to embrittle SiC along regions of residual stresses, opening up thermodynamically and kinetically favorable pathways for fission product escape.

Below we provide a detailed description of project activities and results.

Presentations and Publications

Publications

S. Dwaraknath and G. S. Was, “Development of a multi-layer diffusion couple to study fission product transport in β-SiC,” *Journal of Nuclear Materials*, vol. 444, no. 1, pp. 170–174, 2014.

R. A. Enrique, A. Van der Ven, “Decohesion models of brittle fracture from atomistic simulations: the ab initio tensile test and its relation to nano-rod fracture,” *Physical Review B*, submitted (2014).

R. A. Enrique, A. Van der Ven, “Solute embrittlement of SiC,” to be submitted *Journal of Applied Physics*, (2014).

R. A. Coward, C. R. Winkler, W. A. Hanson, . Jablonski, M. L. Taheri, “TEM Investigation of Ag Ion Implanted β-SiC,” to be submitted to *Journal of Nuclear Materials* (2014).

Presentations

S. Dwaraknath and G. S. Was, “Fission product diffusion in β-SiC using ion implanted multilayer diffusion couples.,” presented at the TMS 2013, San Antonio, TX, 2013.

S. Dwaraknath and G. Was, “Silver Diffusion in PyC Coated β-SiC,” presented at the TMS 2012, Orlando, Fl, 2012

2. Diffusion Couple Development

Several key objectives had to be met in order to develop the diffusion couple. First was obtaining suitable SiC substrates comparable to TRISO SiC. Second was to identify or develop a furnace capable of reach 1600ºC for prolonged conditions in an ultra-high purity argon environment to prevent oxidation of the SiC and prevent excessive surface sublimation that occurs in high temperature vacuum environments. Third was to modify the existing pyrocarbon deposition system to yield consistent depositions. Finally a suitable capping material and deposition process had to be selected.

SiC Substrate Procurement

Three major suppliers were considered for the SiC samples: Rohm and Haas, Coorstek, and Morgan Technical Ceramics. All three provide various grades of CVD 3C-SiC engineered for high and low resistivity, with similar mechanical and thermal properties. The main characteristics of concern for this project are the purity of the CVD SiC and the grain size and shape. The purity of the CVD SiC is important to ensure that the measured diffusion coefficients are characteristic of similar purity CVD SiC used on the TRISO fuel particles. Matching the grain size and shape with the CVD SiC used for TRISO fuel particles is critical in developing accurate diffusion coefficients as well as grain boundary models and distributions.

All three vendors quoted a grain size of roughly 5 microns in length along the growth direction. Rohm and Haas had supplied CVD SiC to us for a previous experiment. Orientation Imaging Microscopy (OIM) had been performed to analyze the grain size distribution for their product. The average size of was approximately 1.5 μm, though there were some grains as large as 15 μm at both surfaces of the CVD SiC plates. The average grain size was smaller than the quoted size, which better mimics the microstructure of the CVD SiC used in TRISO fuel particles. SiC from Rohm and Haas also contains the lowest total impurity concentration in comparison with the other vendors as shown in Table 1.

Table 1. Major impurity concentrations for CVD SiC for three different vendors in ppm.

	B	Ca	Ti	Ni	Se	Cd	Total
Rohm and Haas	0.29	0.84	1.4	0.21	0.10	0.15	3
Coorstek	1.0	0.50	0.50	0.10	0.50	0.50	3.1
Morgan Technical Ceramics	1.5	2.0	0.10	0.50	0.50	0.10	4.7

Furnace Selection and Development

Oxidation problems with a standard tube furnace at 1600°C created the need for a new furnace for the high temperature annealing experiments. A graphite furnace on campus was refurbished and is capable of reaching 2500°C. This temperature is well above what is necessary for the thermal diffusion experiments, which helped prolong the lifetime of the heating elements and aided in preventing sudden loss of temperature in the middle of an experiment. Primary metal gasket seals were cleaned, polished, and reset. All Teflon and other plastic seals were also replaced in order to maintain an inert environment for the tests. Gas lines were switched to stainless steel, as were all valves. An inert gas purifier was added to the argon stream in order to ensure a UHP environment was maintained.

One sample of SiC was heated in this furnace to gauge the level of surface modification that would occur at 1600°C. The sample was inserted into the furnace, the furnace was purged for 1

hour with the UHP Ar, and then it was heated up to 1600°C in 30 minutes. This temperature was held for 10 hours before a 2 hour ramp down to room temperature. The surface was analyzed via Rutherford backscattering spectrometry (RBS) using a 2 MeV He^{++} beam. The RBS measurement revealed a 10 ± 2 nm Si layer on the surface which indicates a decarburization of the surface. Oxygen was not observed within the surface region of interest, suggesting that no oxidation took place. This showed that the furnace should be suitable for the thermal diffusion experiments.

Pyrocarbon Deposition

The previous PyC deposition system took advantage of a horizontal tube furnace as the deposition chamber. Easy access to tube furnaces makes them ideal for initial deployment of chemical vapor deposition (CVD) systems. Unfortunately horizontal tube furnaces also create a geometry in which the deposition conditions change along the hot zone. As a result the depositions are not uniform along the sample. In this geometry the front edge of the sample also served as a turbulence point creating very uneven coatings. As a result of both of these natural features of the system, the usable coating yield was about 10%.

The simple solution to this is to use a vertical geometry where the sample is suspended perpendicular to the reactant flow direction. Unfortunately, this creates the problem of suspending the sample in the hot zone in a manner that does not create too much turbulence in the reactant stream. The graphite furnace used for annealings provided a sample support that kept samples well above the vacuum port and provided a top inlet port with line of sight to the samples as shown in Figure 2. The low placement of the vacuum port with respect to the sample support allows for a vertical flow geometry in the vicinity of the sample. The quartz sight window allows for accurate monitoring of the sample temperature via a pyrometer. This allows for a vertical flow CVD system that provided highly uniform and far more consistent depositions.

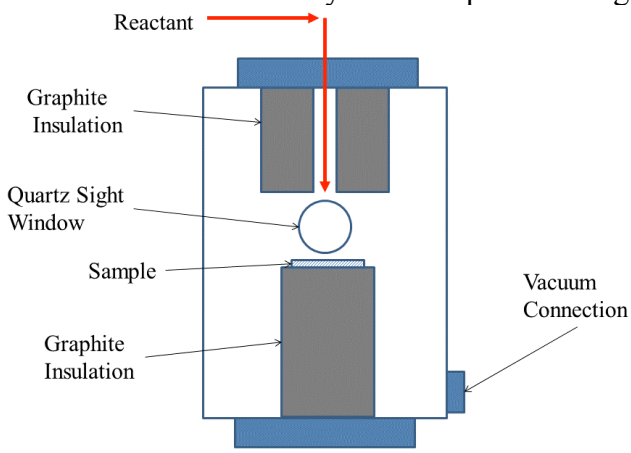

Figure 2. A schematic showing orientation of sample in the graphite furnace with reactant flow and vacuum port.

Several PyC coatings were deposited in the graphite furnace to find the right set of conditions to produce an even PyC coating. An argon flow rate of 50 standard cubic centimeter per minute (sccm), propylene flow rate of 21.6 sccm, overall furnace pressure of 18 Torr, and furnace temperature of 1300°C provided reproducibly even coatings. Several different deposition times were then used to calibrate the coating thickness as a function of time and the coating roughness as a function of time. The coating thickness was measured via RBS. The coating roughness was

measured via atomic force microscopy (AFM). 90µm x 90µm areas were used to provide as much statistical significance as possible. Five scans were performed per sample, one from each corner and one from the center. The maximum calculated roughness was used as the roughness of the coating. Figure 3 shows the calibration for the PyC coating thickness and roughness as a function of deposition time. The deposition thickness data was then fitted with a line, which has a very high confidence with an R of 0.98454. The linear fit does not go through the origin, but gets within fitting error, which makes physical sense. The fit suggests that a 300 nm layer of PyC requires a 52 min deposition.

The areal variation in the deposition rate on the sample support insulation was then tested to see how many substrates could be coated at once using 14 evenly placed substrates. All 14 coatings were optically even with no indications of turbulence. RBS was performed on the first seven to determine thickness. The other seven are symmetrically equivalent. Table 2 shows the measured thickness from RBS, which indicate that the deposition overshot the desired thickness by 3% but the overall variation in the deposition thickness was within the error of the RBS measurement. The 3% error is likely due to a variation in furnace chamber pressure that cannot be resolved with the manometer. This test showed that the deposition rate in the graphite furnace is independent of the position on the sample support insulation, which allowed us to coat multiple samples at a time and prevent sample backlog in the diffusion couple development.

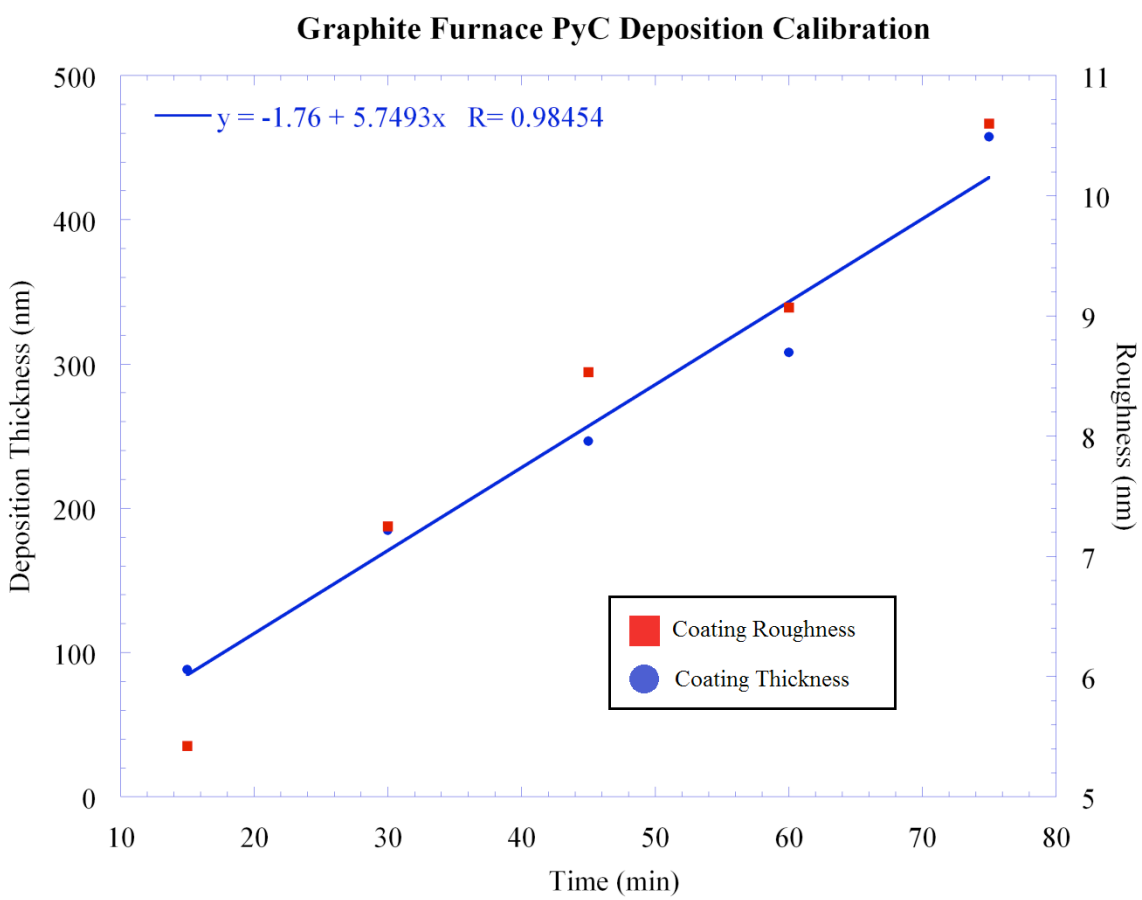

Figure 3. Calibration for PyC thickness and roughness from depositions using the graphite furnace CVD system. The PyC thickness are shown in blue and the roughness is shown in red.

Table 2. PyC thickness for the areal variation test of the graphite furnace based PyC deposition system.

Substrate	PyC Thickness (nm)
1	308 ± 3
2	309 ± 3
3	308 ± 3
4	313 ± 3
5	311 ± 3
6	310 ± 3
7	312 ± 3

Cap Material Selection

Several different materials were tested for their efficacy in preventing FP release from the diffusion couple such that the FP could not diffuse into the SiC substrate. The coatings needed to be high density to server as an effective diffusion barrier and be deposited in a low temperature process to prevent FP diffusion during the coating process. Initial tests involved physical vapor deposition (PVD) of refractory metals (molybdenum and tungsten), which resulted in thin high-density coatings that covered just the surface of the diffusion couples. Due to the large differences in their coefficient of thermal expansion (CTE) in comparison with PyC and weak adhesion between the coating layer and the PyC these layers would easily delaminate during the annealing processing. Sputter deposition SiC was then tested as it has a similar CTE with PyC. Due to geometry of the coating, covering just the front surface, the sputter deposited SiC failed to retain much silver, which was the test FP. A conformal coating was necessary to retain silver in the diffusion couple. Plasma enhanced CVD (PECVD) SiC was chosen as the candidate for a conformal low temperature SiC coating.

The PlasmaTherm 790 PECVD tool in the Lurie Nanofabrication facility (LNF) has both methane and silane as available reactants. As a result, it was possible to deposit PECVD SiC via this tool. A SiC recipe was acquired from Stanford's nanofab. A SiC substrate was then coated with 400 nm of PyC, implanted with silver to a fluence of 10^{16} atoms x cm^{-2}, and then capped with 100 nm of PECVD SiC. It was then annealed for 10 hours at 1100ºC. RBS before annealing indicated that the SiC cap contained trace amounts of oxygen and significant amounts of nitrogen. The oxygen was likely from chamber wall as the tool is also used to deposit oxides. The nitrogen was from the industrial grade argon used as a carrier for the depositions. RBS also indicated that the silver concentration profile did not change as a result of the PECVD SiC deposition. RBS after annealing indicated that approximately 30% of the silver was lost from the diffusion couple, which was significantly better then previous attempts. The incorporation of the nitrogen and oxygen were likely culprits for this loss. While plans are underway at the LNF to introduce higher purity argon to the PECVD tool, they have been slow and are not yet complete.

3. Fission Product Diffusion Experiments

Thermal and Irradiation Behavior in PyC

The behavior of several fission products have been evaluated at 1100ºC in PyC. We have also conducted two experiments to investigate the effect or ion irradiation on both silver and cesium behavior in PyC. Figure 4 shows the geometry of the encapsulated sample design we have developed and the results of thermal and irradiation enhanced diffusion of five FPs (silver, cesium, europium, iodine, and strontium). In Fig. 3a, the orange region to the right is the bulk SiC sample into which diffusion is measured. The grey region is the PyC layer deposited onto

the SiC by CVD, and the thin orange box is the SiC cap deposited by low temperature CVD. The as-implanted profile (dashed white) in Fig. 3a contained approximately 1at% FP at the peak and was implanted at room temperature. Annealing at 1100°C resulted in very different response for the differing FPs. Cesium and iodine broaden, silver moves to the interfaces, while strontium and europium exhibit a combination of these behaviors. These behaviors are consistent with our expectations of the solubility and kinetics of these FPs in PyC from a combination of DFT calculations and phase diagrams from literature: silver has no solubility, cesium has some solubility in PyC but slow diffusion kinetics, and strontium has significant solubility and kinetics in PyC allowing it to be influenced by the PyC/SiC cap interface. Figure 1b shows that indeed, silver does penetrate into SiC to a very shallow depth and forms small particles, consistent with its very low solubility.

Figures 1c and 1d show the dramatic effect of irradiation on diffusion. When an implanted silver sample is heated to 500°C, the distribution narrows, consistent with the low solubility of silver in PyC. However, under irradiation at this same temperature, silver diffuses throughout the entire PyC layer, consistent with enhanced dynamic solubility due to irradiation. For cesium, irradiation was conducted at 1100°C and compared with the result from thermal annealing at that same temperature. Note that while annealing broadens the cesium distribution, irradiation significantly enhances the diffusion, broadening the distribution much further. In both of these cases (silver and cesium), irradiation has a profound effect on the redistribution of the FPs within the PyC.

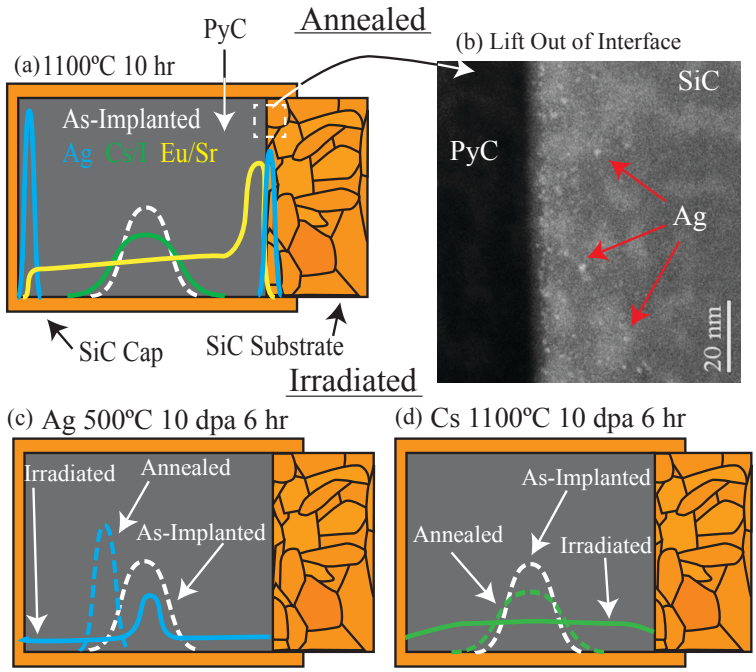

Figure 4. (a) Schematic showing the behavior of various FPs in the heterostructure after an 1100ºC 10 hour anneal. Elements are grouped based on their behavior, which follows the expected solubility from both literature and DFT calculations and range from Ag, which is insoluble in PyC, to Sr which is highly soluble in PyC. (b) TEM lift-out of the sample that contained Ag after annealing showing the diffusion of Ag into SiC in HAADF. (c) Schematic comparing the irradiation behavior to the pure thermal behavior of Ag at 500ºC with evidence of dynamic solubility induced by the irradiation. (d) Schematic comparing the irradiation behavior to the pure thermal behavior of Cs at 1100ºC showing a large increase in the diffusion kinetics under irradiation.

4. Analysis of Fission Product Diffusion

High Resolution Depth Profiling

All of the previous analysis was conducted using Rutherford backscattering spectroscopy (RBS), which is limited in sensitivity to no less then 0.05 at%. In order to measure FP diffusion into SiC, a technique capable of measuring concentration profiles down to the ppm level is necessary. Secondary ion mass spectrometry (SIMS) is capable of resolving FP concentrations down to ppm levels, with depth resolution on the order of a nm.

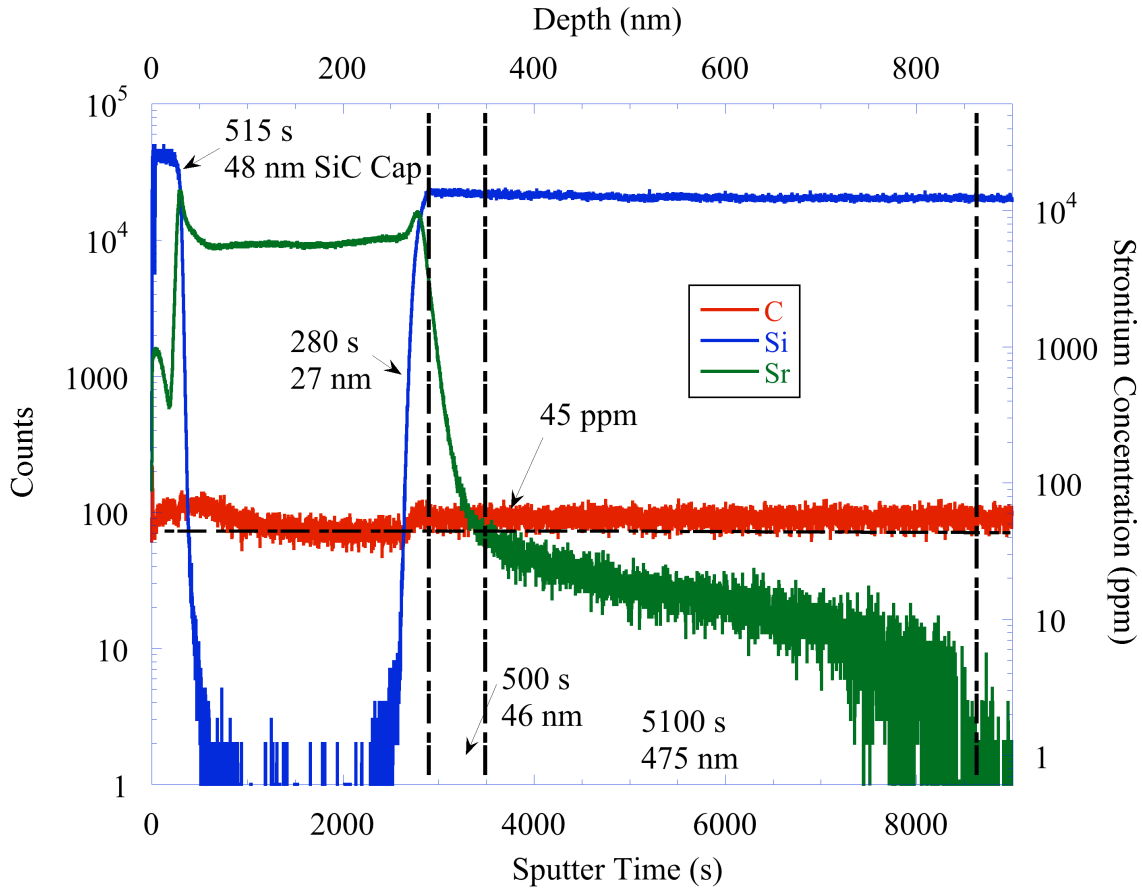

Figure 5. SIMS depth profile for a strontium diffusion couple annealed at 1100ºC for 10 hours. The depth and strontium concentration axes correspond to SiC substrate only, which occurs after approximately 3000s of sputter time after the first vertical dashed black line. The vertical dashed lines define two separate regions in which the strontium diffusion occurs at two different rates. The SiC cap thickness, the full width half-maximum for the PyC/SiC substrate interface, the thickness of first region and second region are all indicated by both the sputter time and the corresponding thickness in nm.

Figure 5 shows a SIMS depth profile for a strontium diffusion couple annealed at 1100ºC for 10 hours. The Si concentration profile allows us to differentiate between 3 layers of the diffusion couple: the PECVD SiC cap that is approximately 50 nm thick, the 300 nm PyC layer in which the strontium was implanted, and finally the SiC substrate. Note the relatively constant concentration of strontium in the PyC, indicating that strontium is still soluble in PyC at the concentrations implanted into the diffusion couple. The strontium concentration increases as it approaches the interface, which could be caused either by segregation to the interface, or an increase in the local chemical potential so that strontium can diffuse into SiC. In the SiC

substrate, it is evident that there are two regions of strontium diffusion. One occurs right after the interface in which the concentration drops two orders of magnitude in less than 50 nm. In the second region, the strontium drops another two orders of magnitude in concentration across nearly 500 nm. TEM analysis of this diffusion couple has failed to find strontium at the interface or in the SiC. We are still searching for a technique that can detect small concentrations of strontium within this diffusion couple with enough spatial resolution to identify the microstructure associated with each region of transport.

5. First-Principles Modeling

Fission product (FP) release rates from TRISO particles are determined by both thermodynamic factors as well as kinetic properties. Figure 6 illustrates a schematic of a spherical SiC shell (the adjacent inner and outer PyC shells have been omitted from the schematic). If steady state conditions are assumed for FP diffusion through the SiC shell, the concentration profile (e.g. of Ag) through the thickness of the shell has a $1/r$ dependence along a radial coordinate. The FP concentration on the inner surface can be determined by assuming a local equilibrium between the inner PyC and SiC. For example, the Ag concentration on the inner surface of the SiC shell will be determined by the equality of Ag chemical potentials in PyC and in SiC

$$\mu_{Ag}^{PyC} = \mu_{Ag}^{SiC} \tag{1}$$

Since the Ag concentration is very dilute in both phases, the chemical potentials can be expressed in terms of the Ag concentration in each phase according to (i.e. Henrian reference state)

$$\mu_{Ag}^{PyC} = \mu_{Ag}^{0,PyC} + kT\ln x_{Ag}^{PyC} \qquad \text{and} \qquad \mu_{Ag}^{SiC} = \mu_{Ag}^{0,SiC} + kT\ln x_{Ag}^{SiC} \tag{2}$$

The Ag concentration in the PyC, x_{Ag}^{PyC}, is determined by the fission process and is in principle a known quantity (input parameter dependent on the properties of the fuel). The equality of the chemical potentials at the PyC/SiC interface according to Eq. 1 allows us then to determine the Ag concentration at the inner surface of the SiC shell after inserting Equations (2) into (1) and solving for x_{Ag}^{SiC}

$$x_{Ag}^{SiC} = x_{Ag}^{PyC} \cdot \exp\left(-\frac{\mu_{Ag}^{0,SiC} - \mu_{Ag}^{0,PyC}}{kT}\right) \tag{3}$$

To determine this concentration though, we must have values for $\mu_{Ag}^{0,PyC}$ and $\mu_{Ag}^{0,SiC}$. These quantities can be estimated using electronic structure calculations based on density functional theory (DFT). To first order, entropic effects due to local vibrational degrees of freedom are neglected. The FP concentration at the outer surface of the shell (at radius R_2) can be assumed to be zero (this will give an upper bound on the FP flux through the shell).

For a steady state concentration profile, the integrated FP flux, F, emerging at the outer surface of the SiC shell is equal to

$$F = \frac{4\pi D C_0}{(1/R_1 - 1/R_2)} \tag{4}$$

where D is the FP diffusion coefficient and C_o is the FP concentration on the inner surface of the SiC shell (number of atoms per unit volume of SiC). The diffusion coefficient is also a quantity that can be estimated from first principles using DFT. The value of D is very sensitive to the diffusion mechanism, depending on whether FP diffusion occurs through the bulk via an interstial, an interstitialacy or a substitutional mechanism, or whether it occurs along grain boundaries or internal cracks.

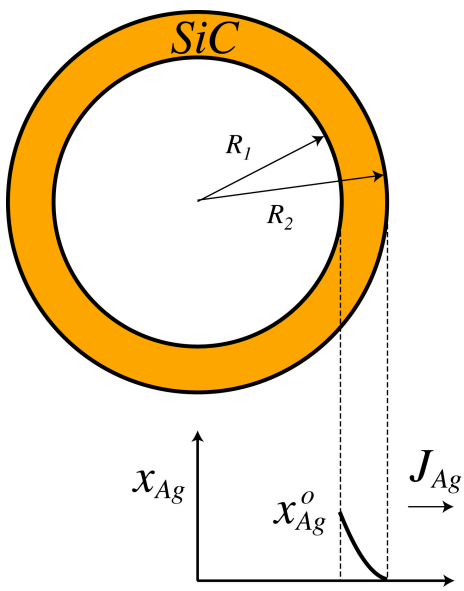

Figure 6: Schematic of a SiC shell with a Ag concentration profile along the radial direction.

During the first year of the project, we calculated thermodynamic properties associated with fission product preference for interstitial sites in SiC, sites at stacking faults, along grain boundaries and on surfaces (relevant if micro-cracks are present). We have also calculated migration barriers associated with fission product diffusion. These results are summarized below.

5.1 Interstitial diffusion

We have calculated thermodynamic quantities for Ag, I, Cs and Sr in PyC and SiC (e.g. the difference between $\mu_{Ag}^{0,PyC}$ and $\mu_{Ag}^{0,SiC}$ as schematically illustrated in Fig. 7) as well as elementary migration barriers for interstitial Ag diffusion in SiC.

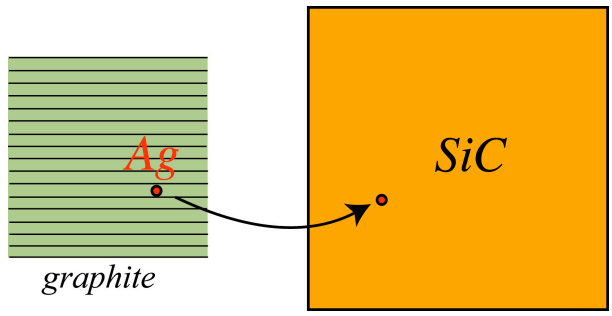

Figure 7: Schematic of the interpretation of the difference in reference chemical potentials $\mu_{Ag}^{0,SiC}$ and $\mu_{Ag}^{0,PyC}$.

In establishing thermodynamic properties of FP solubility in SiC, it is first necessary to determine the sites that FP ions prefer to occupy in SiC. While the SiC shell has the cubic (3C) crystal structure (with an ABC close-packed stacking of Si layers and C layers), it can also contain stacking faults. In fact SiC can form a wide variety of polymorphs, each characterized by a different stacking sequence of close packed planes. The two simplest polymorphs are cubic SiC and hexagonally packed (2H) SiC, the former having Zincblende structure and the latter having a Wurtzite structure. In both these crystal structures, fission products can occupy two distinct types of interstitial sites. We have labeled them A and B. In Wurtzite, A is 6-fold coordinated by Si and by C, while the B site is 4-fold coordinated by Si and C. In cubic SiC, the A site is 6-fold coordinated by Si and 4-fold coordinated by C, while the B site is 4-fold coordinated by Si and 6-fold coordinated by C. The table below lists the site energy of Ag occupying different interstitial sites as calculated with DFT within large supercells (the reference is the energy of Ag in the A site of cubic SiC). The A site is preferred in cubic SiC. Furthermore, the energy increases substantially if Ag is taken from the A site in cubic SiC and inserted into interstitial sites of Wurtzite. This indicates that Ag thermodynamically has a higher solubility in cubic SiC as compared to Wurtzite.

	Site	Relative Energy (eV)
Wurtzite (2H)	A	+1.345
	B	+3.104
Cubic (3C)	A	0.000
	B	+0.925

Table 3: The relative energy of an interstitial Ag in the different sites of cubic and wurtzite crystal structures of SiC.

An interstitial diffusion coefficient in the dilute limit can be estimated analytically once the migration barrier for elementary hops is known. The A-interstitial sites of cubic SiC form an fcc sublattice. The interstitial diffusion coefficient is then equal to $D=2a^2\Gamma$ where Γ is the hop frequency of an interstitial atom and a is the hop distance. Figure 8 shows the energy of an interstitial Ag atom migrating between A sites (passing through an intermediate B site), calculated with the nudged elastic band method as implemented in VASP. The predicted migration barrier is of the order of 1 eV, which is quite low and will result in high interstitial diffusion coefficients, especially at high temperature. Nevertheless, the concentration of Ag atoms in SiC is very low, resulting in low total fluxes, as will be discussed below.

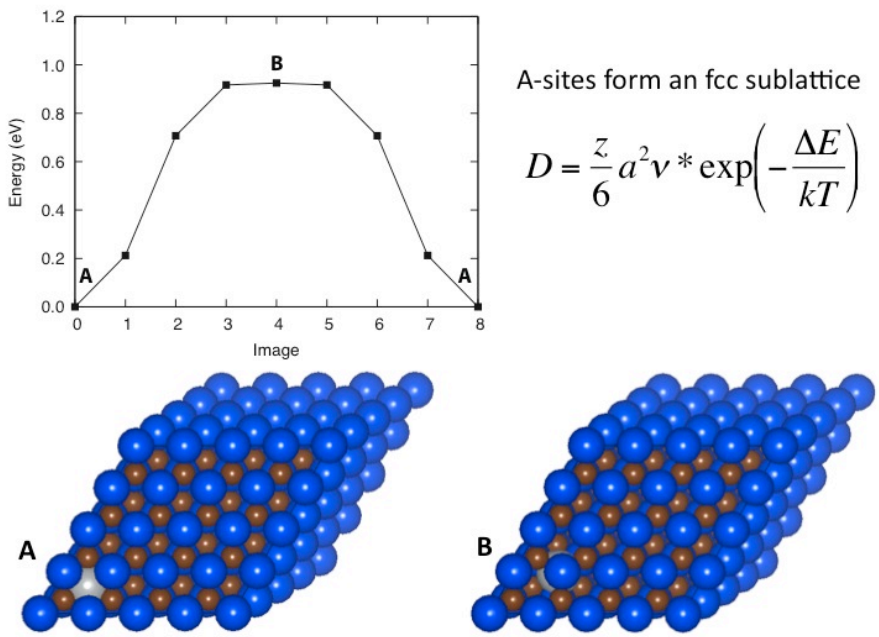

Figure 8: Calculated migration barrier for interstitial Ag diffusion in cubic SiC from an A site through an adjacent B site (see text for description). The A sites in cubic SiC form an fcc sublattice. Analytical expressions for interstitial diffusion coefficients (in the dilute limit) can be evaluated once the migration barrier ΔE is known or calculated (~1eV in this case). In the above equation, z is the coordination number of the fcc sublattice, a is the hop distance and ν is a vibrational prefactor (~10^{13} Hz).

We have also investigated the site energies of other fission products in cubic SiC, including I, Cs and Sr. The table below lists the difference in energy between B-site occupancy and A-site occupancy in cubic SiC. I behaves similarly to Ag. Cs prefers the B-site over the A-site, although the energy difference is only 25 meV, which is a negligible difference at high temperature. Sr, while preferring the A site, only has a small energy penalty to overcome to occupy the B site. These results imply that I will have a similar interstitial diffusion coefficient as Ag, while Cs and Sr should have significantly higher interstitial diffusion coefficients.

Site Energies in SiC-3C Supercell

Interstitial atom	$E_B - E_A$ (eV)
Ag	1.094
I	1.027
Cs	−0.026
Sr	0.123

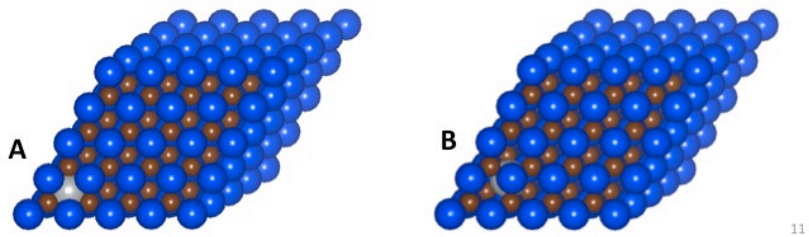

Figure 9: Site energy difference for various fission product elements in cubic SiC.

While Cs and Sr seem to have higher interstitial mobilities (due to smaller site energy differences between A and B sites), we must also determine their solubilities in cubic SiC to estimate their flux through a SiC shell. The table below lists the change in energy of taking a FP from their pure crystalline state and inserting it into an isolated interstitial site of the SiC crystal.

SiC Interstitial	ΔE (eV)
Ag	9.897
I	21.654
Cs	24.450
Sr	15.628

Table 4: Solution energies of associated with taking a fission product atom from its crystalline pure state into an interstitial site within the SiC crystal structure.

As is clear from this table, the energy increases quite substantially when taking I, Cs and Sr from their pure crystalline state and inserting them as isolated atoms in the interstitial sites of SiC. Morgan, Szlufarska et al [6] investigated a wide variety of substitutional defects involving fission products such as Cs and also found very high solution energies (ranging between 9 and 11 eV), although substantially lower than the interstitial solutions energies reported in table 4. These results imply that these elements will have exceedingly low solubilities in SiC. More realistically, in the context of triso particles, solubility should be established between SiC and PyC (or graphite). This can be represented compactly in ternary phase diagrams as illustrated below. The ternary phase diagrams consist of three elements, C, Si and the FP (= Ag, I, Cs and Sr). SiC is a

compound in this ternary phase diagram, while PyC (approximated as ABAB stacked graphite) is a corner of the ternary composition space. In the diagrams below, we summarize formation energies of various compounds and dilute interstitial configurations. Of interest is that Cs and Sr form stable compounds with carbon (negative formation energies for CsC_6 and SrC_6). The PyC is therefore likely a gettering medium for Cs and Sr.

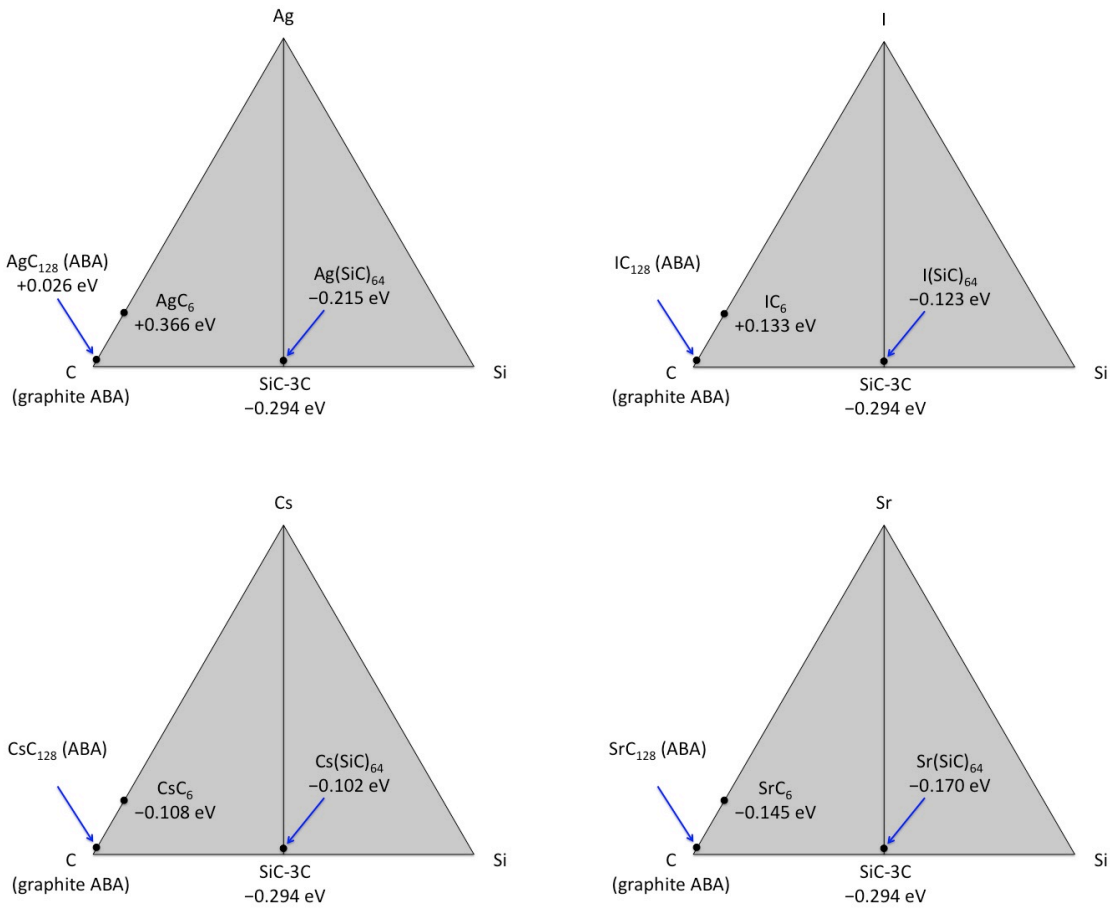

Figure 10: The equilibrium FP distribution across the interface between PyC and SiC can be represented in a ternary phase diagram consisting of C, Si and the FP. The SiC phase is compound in this composition space while PyC is in the C-corner. The diagram also allows a representation of FP stability within graphite. For example, the negative formation energies for CsC_6 and SrC_6 indicate that carbon (graphite with AA stacking) will getter these fission products.

Ultimately, we are interested in the release rate of FP through the SiC shell. This is determined by Equation 4, which depends on the solubility of the FP at the inner surface of the SiC shell when in contact with PyC and the diffusion coefficient for FP transport through cubic SiC. So far, we have only calculated a migration barrier for interstitial diffusion in the bulk. Inserting calculated values for $\mu_{Ag}^{0,PyC} - \mu_{Ag}^{0,SiC}$ into Eq. (3) and a migration barrier in the expression for the interstitial diffusion coefficient into Eq. (4), we can predict the FP release rate, F, from a triso particle. The result, assuming interstitial solubility in the bulk and interstitial bulk diffusion, is plotted in Fig. 11. The prediction, when compared to experimental measurements, clearly shows

that Ag release is significantly under predicted if bulk solubility and bulk interstitial diffusion is assumed.

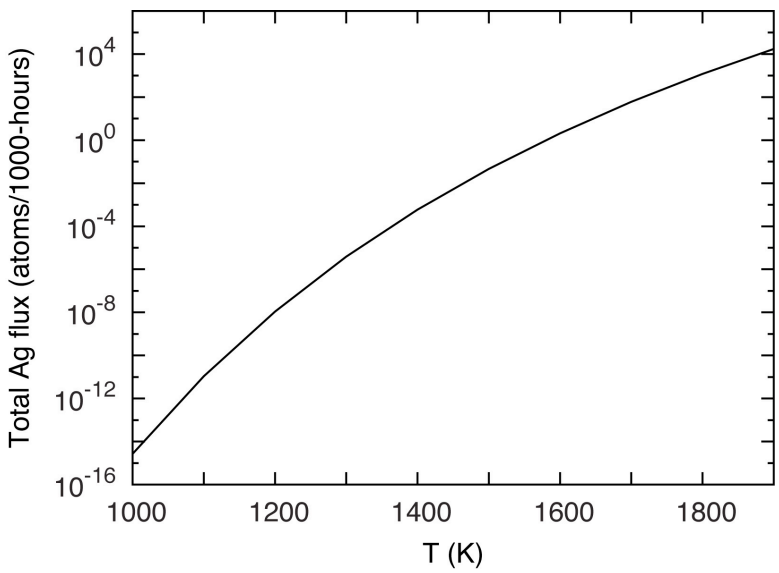

Figure 11: Calculated Ag release rate from a triso particle as predicted using Eq. (4) and using calculated thermodynamic and kinetic data. In this prediction, only interstitial Ag solubility and interstitial Ag diffusion in bulk SiC is assumed. Solubility and transport properties along internal surfaces and grain boundaries are significantly higher as described below.

The result of Figure 11 strongly suggests that bulk diffusion is highly unlikely as the mechanism with which Ag passes through the SiC shell. Nevertheless, the migration barrier for interstitial Ag diffusion in SiC is predicted to be quite low (~1 eV). The bottleneck is getting Ag into the SiC as manifested by the Ag concentration at the inner surface of the SiC shell according to Eq. 3. The energy to take Ag from graphite to an interstitial SiC site is predicted to be of the order of 6-7 eV, resulting in very low equilibrium Ag concentrations on the inner surface of the SiC shell.

The solubility of Ag along grain boundaries and internal surfaces is significantly higher as described below.

5.2 Grain boundaries

While our first-principles calculations as well as those by Morgan and Szufarska et al [6] indicate that that fission product escape through bulk diffusion is not likely, it may nevertheless occur along short-circuit pathways such as grain boundaries. Experimental evidence clearly shows that the SiC layer of a TRISO particle is polycrystalline and therefore contains grain boundaries [7]. We expect these boundaries to be a less constrained environment for diffusing fission products than the bulk, but more constrained than microcracks. The model that we chose to use for this system is the symmetric tilt grain boundary (STGB) [7]. This model starts with a mirror plane in the crystal and rotates the two halves on either side of this plane to create a coincident site lattice (CSL) [8]. For SiC-3C, one of these mirror planes is (110).

After rotation, we shifted one half of the boundary by 0.5 unit cells in both in-plane directions, in order to create a configuration with lower energy. The extreme low-angle limit of this type of boundary is the informally designated Σ1 boundary, which is composed of a series of edge dislocations separated by wide regions of near-perfect alignment of the two halves of the grain boundary. Our choice of distances to shift was determined by the crystal alignment needed to achieve a Σ1 boundary in the low-angle limit.

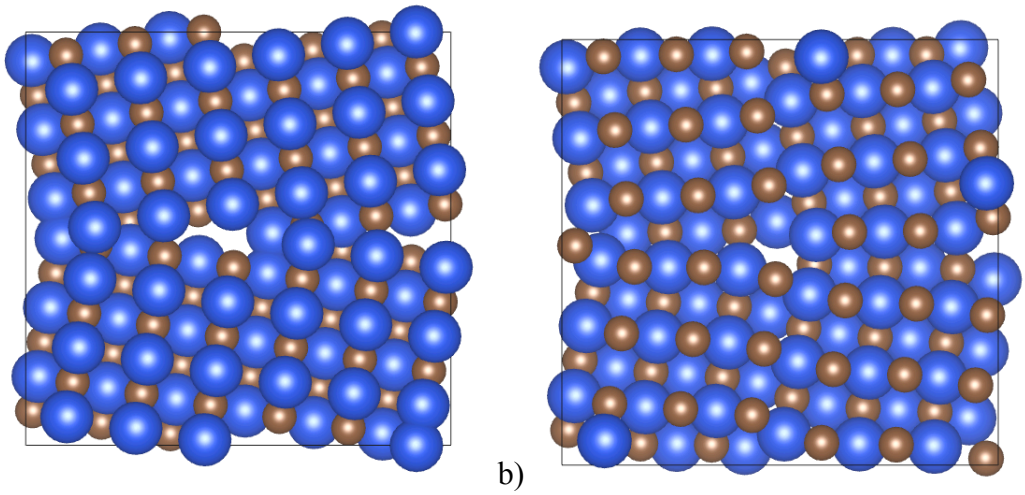

Figure 12. A Σ37 symmetric tilt grain boundary a) before relaxation and b) after relaxation using DFT.

We have tested the formation energy for Ag in the Σ37 and Σ41 grain boundaries. The results (Table 5) show that the formation energy is larger than for the C-rich (100) surfaces, but much less than the ~10 eV for an interstitial in bulk SiC-3C. There is also a trend in higher-angle grain boundaries having less of an energy penalty than low-angle boundaries, which is probably due to the former having larger gaps and therefore a less constrained environment for the Ag atom.

Slope	Sigma	Energy (eV)
1:9	41	4.662
1:6	37	4.169

Table 5. Formation energies for Ag in SiC-3C grain boundaries.

Nevertheless, the energy of taking a Ag atom from pure Ag (precipitated metallic state) or from graphite to a site along one of the above considered grain boundaries is still positive, indicating that there is no energetic driving force for Ag to segregate to SiC grain boundaries if it is already in the metallic state or intercalated within graphite.

5.3 Surfaces

We also explored the thermodynamics of fission product segregation to surfaces that will exist if micro-cracks are present. SiC has both Si-rich and C-rich surface reconstructions. The Si-rich surface is (2x1) and has either pairs of Si atoms tilted toward each other, or else true dimers as on Si (1 0 0). The C-rich surface has carbon dimers in either a (2x1) or *c*(2x2) arrangement. The stable reconstruction in a particular case may depend upon local surface stress. Figure 13 shows these reconstructions.

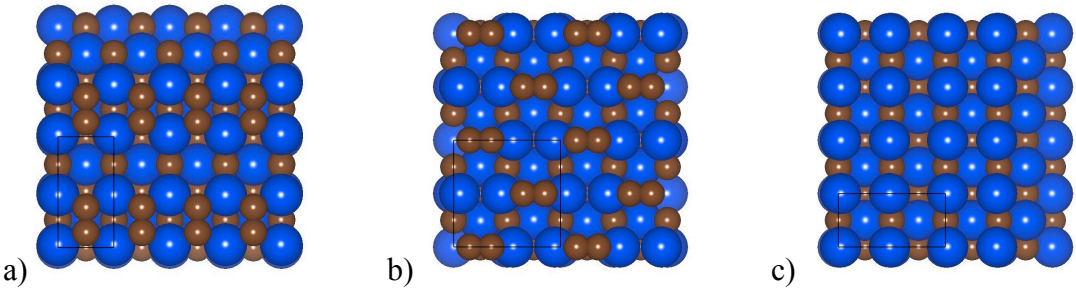

Figure 13. (1 0 0) surface reconstructions for a) C (2x1), b) C *c*(2x2), and c) Si (2x1).

We have done calculations for Ag on both Si-rich (2x1) and C-rich (2x1). We find that adsorbed Ag has a formation energy near +2.0 eV for different sites on the carbon-rich surface, and at −1.246 eV for one site on the silicon-rich surface (Table 6). This last result indicates that there is a thermodynamic driving force for Ag to segregate to Si-rich surfaces.

Surface	Site	Energy (eV)
C (2x1)	1	1.974
C (2x1)	2	2.001
C (2x1)	3	2.050
Si (2x1)	1	−1.246

Table 6. Formation energies for adsorbed Ag on different sites and surfaces of SiC-3C (1 0 0).

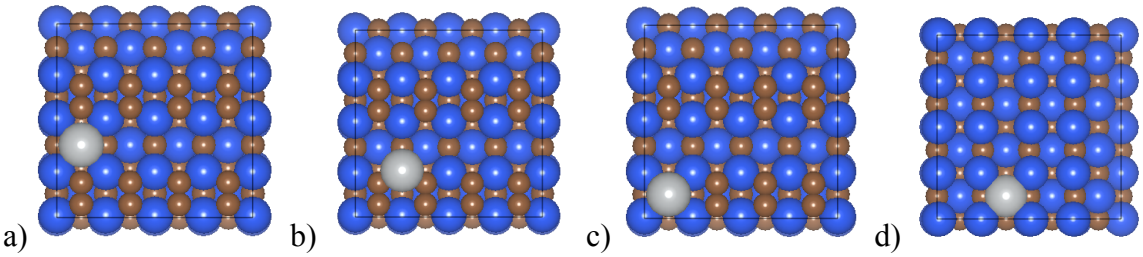

Figure 12. SiC-3C (1 0 0) surface sites: a) C (2x1) 1, b) C (2x1) 2, c) C (2x1) 3, d) Si (2x1) 1.

We have also calculated formation energies for the adsorption of I, Cs, and Sr on the lowest energy site: Si-rich (2x1), site 1. These formation energies are negative and even more favorable than for Ag (Table 2).

Adsorbate	Site	Energy (eV)
Ag	1	−1.246
I	1	−2.280
Cs	1	−2.331
Sr	1	−3.205

Table 7. Formation energies for different fission products adsorbed on the (2x1) silicon-rich (1 0 0) surface of SiC-3C.

Although the Si-rich surfaces are most favorable for adsorption, the TRISO particles are a carbon-rich structure, and so it may be more likely that microcracks in the SiC layer have carbon-rich surfaces. Even if so, the positive formation energy for adsorption of Ag is much smaller than for insertion into the bulk (~10 eV) and along grain boundaries (~4.5 eV), and so a surface-like mechanism (microcracks or grain boundaries) may account for the major diffusion path.

We also calculated the formation energy for the insertion of Ag into AB-stacked graphite to be 3.034 eV. Using graphite as a model for the inner PyC in the TRISO pellets, we expect that it is thermodynamically favorable for Ag to migrate from the PyC to any SiC surface, including carbon-rich surfaces (where adsorbed Ag has a formation energy near 2.0 eV).

Analogous to the study of Ag adsorption energies to SiC surfaces, we also calculated the formation energies for Cs, I and Sr adsorbed onto SiC (100) surfaces. Table 8 shows the formation energies for four fission products on SiC (100). We labeled the surface sites according to Ref. [9].

Surface	Site	Ag	Cs	I	Sr
C (2x1)	1	1.974	−1.588	−0.242	−0.756
C (2x1)	2	2.001	−1.637	−0.223	−1.868
C (2x1)	3	2.050	−1.436	0.498	−1.065
Si (2x1)	1	−1.246	−2.331	−2.280	−3.205

Table 8. Formation energies (in eV) for Ag, Cs, I, and Sr on (100) surfaces of SiC-3C.
Cs, I and Sr show formation energies qualitatively different from that of Ag. Cesium and strontium bind favorably (relative to the pure element reference states) to all of the surfaces and sites studied here, while Ag binds favorably only to the Si-rich surface. Iodine is favorable in all locations except for one of the sites on the C-rich surface.

In summary, the flux through TRISO particles at the continuum level depends on the inner surface fission product concentration, which is determined by

$$x_{Ag}^{SiC} = x_{Ag}^{PyC} \cdot \exp\left(-\frac{\mu_{Ag}^{0,SiC} - \mu_{Ag}^{0,PyC}}{kT}\right)$$

First-principles estimates for the difference $\mu_{Ag}^{0,PyC} - \mu_{Ag}^{0,SiC}$ in the bulk and at grain boundaries ranges from 7 eV (bulk) to ~1 eV (grain boundaries). First-principles calculations predict that Ag has a driving force to precipitate out as metallic Ag particles when it is present in graphite, in SiC or along grain boundaries in SiC. Only Si-terminated surfaces exhibit an energetic attraction for Ag relative to the metallic state. This result indicates that a likely fission product escape pathway is along freshly created SiC surfaces. We therefore next explored how cracks may form in SiC, focusing in particular on the embrittling potential of Pd.

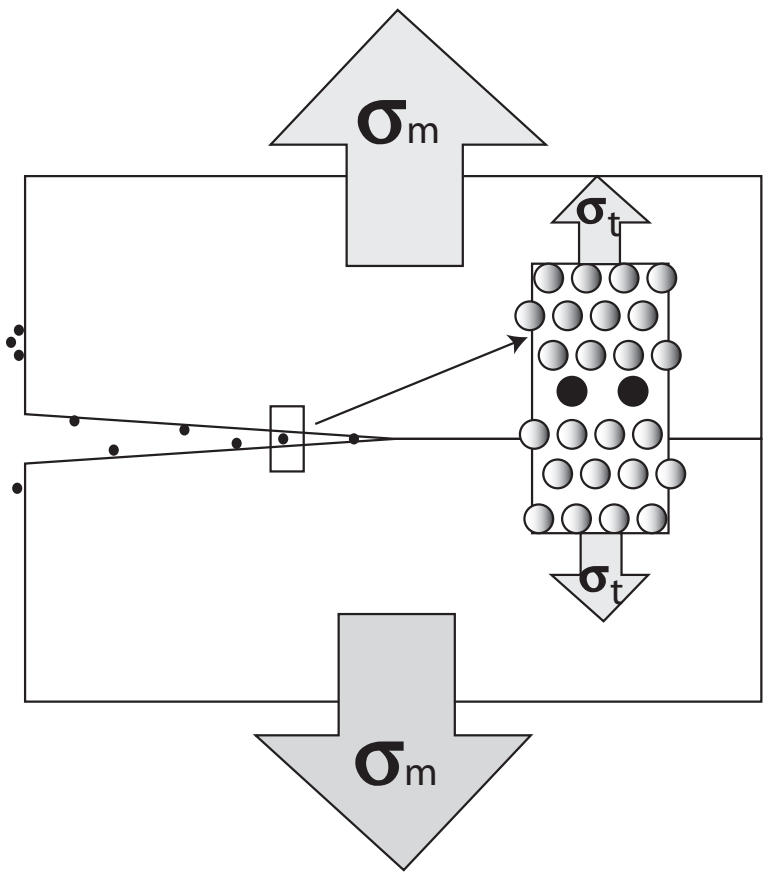

Figure 13: Schematic illustration of embrittlement by Pd of a transgranular crack in SiC.

5.4 Decohsion in SiC and the embrittling effect of Pd

SiC is brittle and has very little susceptibility to plastic deformation through dislocation glide. Intergranular and transgranular crack propagation will therefore occur with minimal if any crack tip blunting due to plasticity. The geometry of for example a transgranular crack will be very sharp as schematically illustrated in Fig 13. While the atomic planes ahead of the crack tip are crystallographically identical to the atomic planes in the crystal adjacent to the crack path, they are nevertheless subjected to a higher normal stress due to the broken symmetry resulting from the presence of the crack. The absence of plasticity during crack propagation makes it possible to analyze the energies and stresses at the crack tip with a cohesive zone model describing the response of the crystal along the planes ahead of the crack tip. The total response of the crystal containing a crack can then be modeled by combining the cohesive zone model with a description of bulk elasticity for the regions adjacent to the crack path. The slow variation in the crack opening behind and ahead of the tip ensures that at the atomic level there is very little inclination between the decohering atomic planes. At the atomic scale, therefore, decohesion can be viewed as the separation of parallel crystallographic planes. This makes the parameterization of a cohesive zone model amenable to first-principles electronic structure approaches by isolating a microscopic element as shown in Fig 13, which is subject to a local value of deformation and stress σ.

Formally, the cohesive zone model should describe the response of the decohering region to externally imposed loads or displacements. This information can be encapsulated within a

function that describes the dependence of the energy, e, of the decohering zone on a metric of separation δ. The derivative of this energy with respect to separation will then yield a traction-separation curve. In formulating a cohesive zone model and its accompanying energy versus separation relationship, it is necessary to exercise care when defining the cohesive zone energy and the cohesive zone separation δ. In the course of this project, we developed a rigorous thermodynamic formalism to extract a cohesive zone model from first-principles electronic structure calculations of decohesion. This was used to construct cohesive zone models for SiC and SiC in the presence of Pd.

We explored the possibility of developing a universal binding curve for covalent crystal structures such as SiC, similar to the universal binding curves for metals. To construct an extension to the metal universal binding energy relationship (UBER), let us start by considering the expression for the force between the two separating parts. By differentiating UBER with respect to distance we obtain

$$\sigma(\delta) = \frac{d\,e(\delta)}{d\delta} = \frac{2\gamma_\infty \delta}{\lambda^2}\exp\left(-\frac{\delta}{\lambda}\right) \qquad (5)$$

Here we can interpret the force as the multiplication of two terms. On the left part we have an elastic component stating that the force is proportional to the elongation, while on the right hand there is a term representing an exponential decay. In a sense, we can argue that these are the two minimum ingredients that would be required to describe the force.

At small displacements, the force has to be elastic. On the other hand, as we break the solid into separate parts, the only form of binding will come from the tail of the wave function of the electrons, which will in general have the shape of a decaying exponential. This is a general feature of the electron density, and is a characteristic invoked by Banerjea and Smith [10] to explain the origin of the UBER and its broad range of applicability.

If the exponential term is an essential result of density functional theory, we might seek to improve on UBER by allowing for nonlinearities in the elastic part of the force, by adding a quadratic, cubic, etc. terms.

$$\sigma(\delta) = \frac{2\gamma_\infty}{\lambda}\left[\frac{\delta}{\lambda} + B\left(\frac{\delta}{\lambda}\right)^2 + C\left(\frac{\delta}{\lambda}\right)^3 + \ldots\right]\exp\left(-\frac{\delta}{\lambda}\right) \qquad (6)$$

The extended expression of the force can then be integrated to recover the new binding-energy relationship, which can then be rearranged in the form:

$$e(\delta) = 2\gamma_\infty\left[1 - \left(1 + \frac{\delta}{\lambda} + \alpha_2\left(\frac{\delta}{\lambda}\right)^2 + \alpha_3\left(\frac{\delta}{\lambda}\right)^3 + \ldots\right)\exp\left(-\frac{\delta}{\lambda}\right)\right] \qquad (7)$$

Notice that we have chosen to write the expression in a way that the idea of an effective length λ is retained, so this expression can still be useful when studying universality in the binding-energy relationship. At the same time, it is general enough to allow for a suitable fit of the traction curves.

In Figure 14 we show the results of fitting Eq. 7 to first-principles calculated traction curves. In We can see from the figure that the extended form of the binding curve can indeed reproduce very well the numerical data from the simulation.

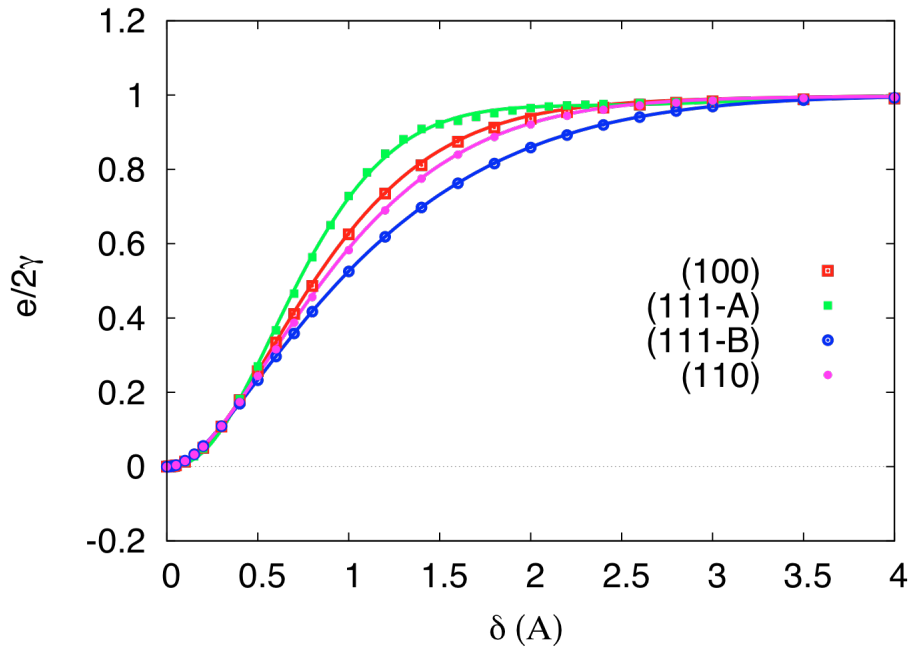

Figure 14: Fit of the simulation data of Fig. 11 with the extended expression for the binding-energy relationship, Eq (7). Points represent VASP calculations while solid lines are the result of the fit.

We next investigated the role of Pd in embrittling SiC. The equilibrium state of the cohesive zone when subjected to a constant Pd chemical potential and stress is determined by the minimum of the grand force potential,

$$\phi(\sigma,\mu_{Pd}) = e - \sigma\delta - \mu\theta \qquad (8)$$

where μ_{Pd} is the Pd chemical potential and θ is the Pd concentration between the decohering planes. Given parameterizations for $e(\delta)$ and for $\delta(\sigma)$ it is possible to calculate a grand force potential according to Eq. (8). We consider two possible states within the cohesive zone: (i) pure SiC without any impurities and (ii) a cohesive zone with all TC or TSi tetrahedral sites filled with Pd. Figure 15 shows the variation of grand force potentials for the two cases as a function of stress σ. The grand force potential shown in Figure 15 was evaluated by setting the Pd chemical potential equal to that of metallic Pd. This implies that decohesion occurs next to a reservoir of precipitated metallic Pd.

The grand force potentials for each state within the cohesive zone first decrease having a negative curvature until a maximum stress is reached, upon which the grand-force potentials increase with positive curvature as the stress is decreased form its maximum value. The curvature of the grand force potential is related to minus the compliance of the cohesive zone. A negative curvature indicates a regime where the cohesive zone is mechanically stable, while a

positive curvature indicates a negative compliance and thus a cohesive zone that is mechanically unstable.

Figure 15 shows that at zero stress, the state of the cohesive zone with the lowest grand force potential corresponds to pure SiC. However, the slope of the grand force potential for the cohesive zone saturated with interstitial Pd is more negative. This causes the grand force potential for the Pd saturated cohesive zone to cross that of pure SiC at a stress substantially below the maximum stress of the pure SiC cohesive zone. The crossing of free energies for distinct states (or phases) signifies a thermodynamic driving force for a first-order phase transformation. In the present example, the crossing of the grand force potentials at σ_{tr} indicates a thermodynamic tendency for a stress induced phase transformation within the cohesive zone, where Pd fills the interstitial sites within the cohesive zone. The equilibrium state within the cohesive zone will be determined by the minimum envelope of the grand force potential as a function of stress.

We can also plot the traction curve of the cohesive zone at constant Pd chemical potential corresponding to the equilibrium state as determined by the minimum envelope of the grand force potential. This is shown by the dark line in Figure 16. Once the transformation stress σ_{tr} of ~16GPa is reached the separation increases discontinuosly to the traction curve for the Pd saturated cohesive zone. This discontinuous increase in separation is accompanied by an influx of Pd within the cohesive zone. As is clear from Fig. 16, the maximum stress for decohesion of the Pd saturated cohesive zone is substantially lower than that of pure SiC. Hence the stress induced transformation within the cohesive zone, accompanied by an influx of Pd, leads to an embrittlement of SiC.

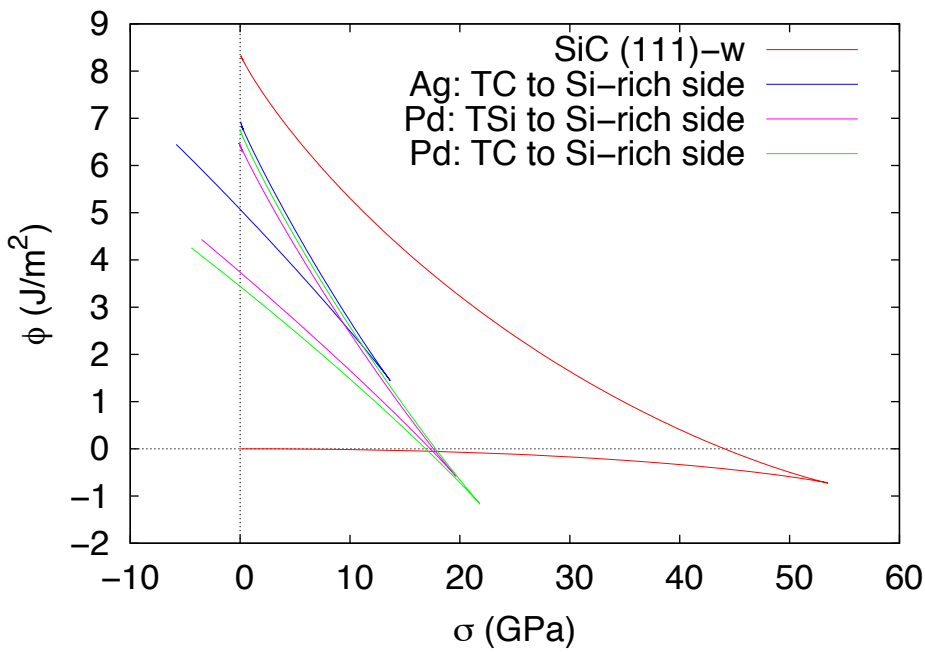

Figure 15: Grand force potential (free energy) of a cohesive zone (pair of (111) planes in SiC) at constant Pd chemical potential as a function of stress. The plot shows that above ~16 GPa, the cohesive zone saturated with interstitial Pd (green curve) becomes thermodynamically more favorable than the pure SiC cohesive zone at Pd chemical potentials coinciding with that of metallic fcc Pd.

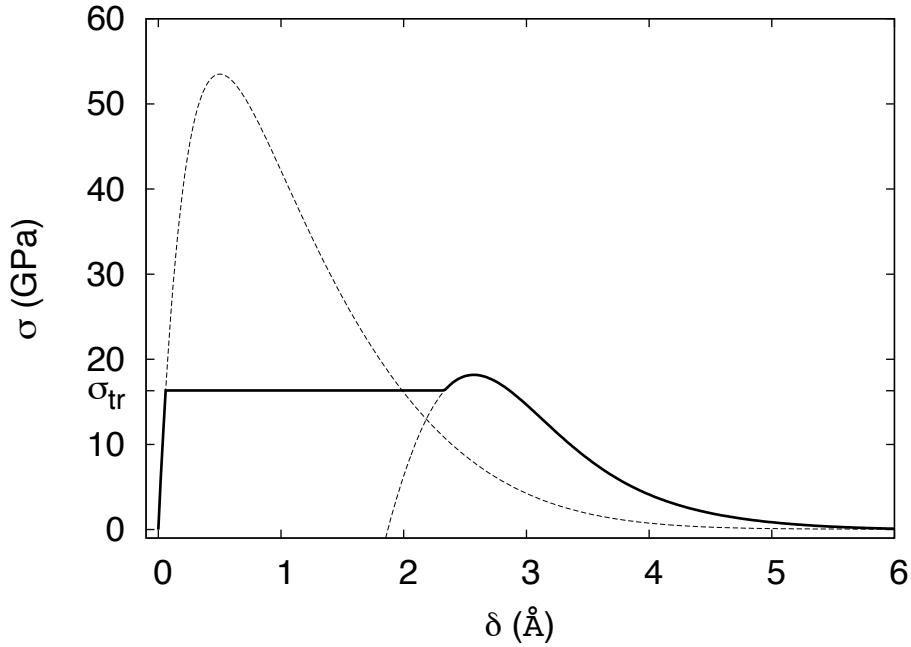

Figure 16: Traction curve for SiC decohesion along a pair of (111) planes in the absence of Pd and SiC with the decohering plane saturated with Pd. The dark solid line corresponds to the equilibrium traction curve determined by the envelope of the grand force potential of Fig. 15. The maximum stress for decohesion is substantially lower than that for SiC in the absence of Pd.

These results suggest the following mechanism with which fission products can escape through the SiC shell. The presence of Pd, as a result of fission, makes SiC susceptible to crack opening in regions of high residual tensile stresses. The tensile stresses can emerge during growth or as a result of large temperature gradients. If the residual stresses at the crystallographic level are greater than the maximum stress of decohesion when Pd segregates to the cohesive zone, cracks will propagate. These cracks can serve as short-circuit diffusion paths for fission product escape. Ag, for example, has an energetic driving force (as predicted from first principles, see section 5.3) to adsorb to the Si-rich surfaces that form upon decohesion. Furthermore, Ag readily alloys with Pd, indicating an energetic attraction to Pd atoms.

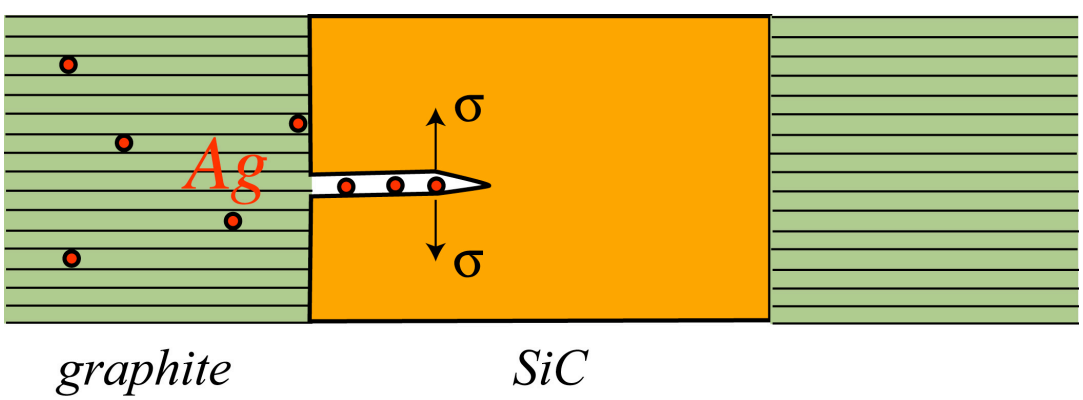

Figure 17: Schematic illustration of Pd induced embrittlement mechanism to produce short-circuit fission product diffusion pathways.

References

[1] R.R. Hobbins, D.A. Petti, P.A. Demkowicz, R.N. Morris, in:, VHTR R&D Meeting 2013, Idaho Falls, ID, 2013.
[2] T.N. Tiegs, Fission Product Pd-SiC Interaction in Irradiated Coated Particle Fuels, 1980.
[3] P.A. Demkowicz, B. Collin, in:, VHTR R&D Meeting 2013, Idaho Falls, Id, 2013.
[4] I.J. van Rooyen, D.E. Janney, B.D. Miller, P.A. Demkowicz, J Riesterer, in:, Htr 2012, 2012.
[5] R.N. Morris, in:, VHTR R&D Meeting 2013, Idaho Falls, ID, 2013.
[6] D. Shrader, I. Szlufarska, D. Morgan, Journal of Nuclear Materials 421, 89-96 (2012).
[7] L. Tan, T. R. Allen, J. D. Hunn, and J. H. Miller, *J. Nuclear Mat*. **372**, 400 (2008).
[8] M. Wojdyr, S. Khalil, Y. Liu, and I. Szlufarska, *Modelling and Simulation in Mat. Sci. Eng.* **18**, 075009 (2010).
[9] P. C. Schuck and R. E. Stoller, *Phys. Rev. B* **83**, 125303 (2011).
[10] Banerjea, A and Smith J.R. Phys. Rev. B 37, 6632 (1988)